ACS Photonics

Article

pubs.acs.org/journal/apchd5

Near-Field Fano-Imaging of TE and TM Modes in Silicon Microrings

Federico La China,*[,†,‡] Francesca Intonti,[†,‡] Niccolò Caselli,[†,‡] Francesco Lotti,[†,‡] Francesco Sarti,[†,‡] Anna Vinattieri,[†,‡] Adrien Noury,[§] Xavier Le Roux,[§] Weiwei Zhang,[§] Eric Cassan,[§] Carlos Alonso Ramos,[§] Elena Durán Valdeiglesias,[§] Nicolas Izard,[§,∥] Laurent Vivien,[§] and Massimo Gurioli[†,‡]

[†]European Laboratory for Non-Linear Spectroscopy, 50019 Sesto Fiorentino (FI), Italy

[‡]Department of Physics and Astronomy, University of Florence, 50019 Sesto Fiorentino (FI), Italy

[§]Institut d'Electronique Fondamentale (IEF), Université Paris 11, CNRS UMR 8622, F-91405 Orsay, France

[∥]Laboratoire Charles Coulomb, CNRS-UMR 5221, Université Montpellier, 34000 Montpellier, France

ABSTRACT: A deep-subwavelength imaging of the optical-guided modes localized in silicon microring resonators, obtained with a polarization-sensitive Fano-imaging technique, is demonstrated. We merge together near-field scanning optical microscopy and resonant forward scattering spectroscopy, leading to near-field hyperspectral imaging without the need of embedded light emitters or evanescent light coupling into the microring. The combined analysis of the observed Fano-like spectral line shapes and of the near-field intensity spatial distributions, supported by accurate numerical calculations, gives a clear discrimination between the TE and the TM modes.

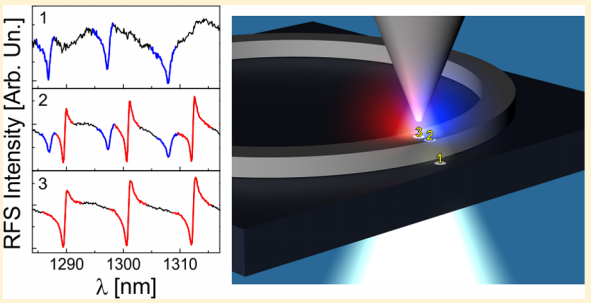

KEYWORDS: *silicon microrings, near-field optics, resonant scattering, Fano resonances*

Microresonators have been attracting considerable attention for the last decades concerning photonic applications, from sensors to quantum electrodynamics effects based devices. High quality factor (Q) nanophotonic systems exhibit a very low laser threshold and induce Purcell effect, or even Rabi splitting in the strong coupling regime, whenever the emitter is placed in the high electric field region.[1−6] For sensing applications, it is crucial to observe the resonance spectral shift due to the mode interaction with the detecting object, which is maximized in the region where the electric field of the mode is more tightly localized.[7,8] Finally, integrated optical switching devices based on microresonators exploit the mode overlap with the input and output waveguides for tailoring the photon hopping between interacting resonators.[9−11] It follows that a precise knowledge of the electric field distributions into photonic structures is of the utmost relevance in several branches of photonics.

Among different kinds of resonators, silicon microrings formed by a closed circular waveguide have been largely used for photonic applications due to the strong light confinement that can be achieved within silicon structures and the availability of electronics fabrication facilities to realize photonic integrated circuits.[12] In such resonators, optical waves are efficiently guided along the ring for both TE polarization (electric field parallel to the ring plane) and TM polarization (electric field perpendicular to the ring plane), which gives an additional degree of freedom with respect to photonic crystal microcavities on a slab where the TE modes dominate. The spectral spacing of the resonant modes can be easily adjusted by varying the ring diameter and the waveguide geometry, thus giving the possibility to precisely tune the resonances at specific wavelength targets. In order to optically investigate such devices, light can be either efficiently loaded or extracted through evanescent coupling.[13−15] Therefore, microring resonators have been exploited for add-drop filters and high-order, dense wavelength filtering in integrated optics,[16−18] and even as efficient sources of entangled photon pairs.[19] Standing waves in individual ring resonators allow for coupling the resonant modes to emitters deposited on the ring, such as single-wall carbon nanotubes,[20,21] with the advantage of exploiting the large mode volume to increase the number of emitters in view of optoelectronic devices. The presence of both TM and TE modes may also lead to the possibility of dealing with either electric or magnetic emitters.[22] Finally, TM modes suffer different propagation losses than TE modes, associated with their different overlap with vertical and horizontal sidewall roughness.[12,23] This unavoidable effect, due to the nature of lithography fabrication processes, gives a different response in microrings for the TE and TM modes, and many efforts have been directed to discriminate the two orthogonal states.[24]

Despite the relevance of the mode mapping issue and the concomitant large use of microring resonators in photonics, very few studies of the TE and TM mode imaging in microrings have been reported in the literature. On one side, for materials such as TiO_2, Si_3N_4, polymer, and Si, the quite poor (if any) optical emission from the bulk material makes useless the common photoluminescence-based methods for hyperspectral

Received: June 15, 2015
Published: November 17, 2015

ACS Publications © 2015 American Chemical Society

DOI: 10.1021/acsphotonics.5b00327
ACS Photonics 2015, 2, 1712−1718

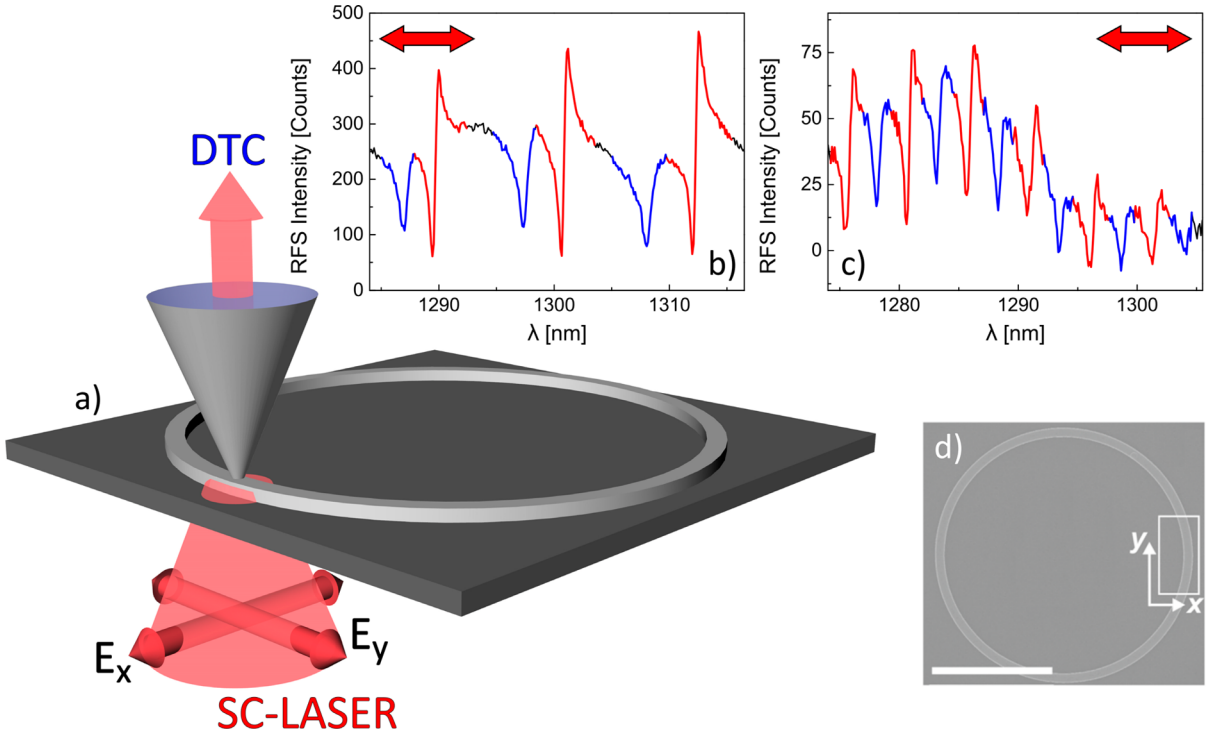

Figure 1. Experimental configurations and resonant scattering data. (a) Schematic view of the experimental setup: a room-temperature SNOM is used in transmission geometry to detect the resonant forward scattering (RFS) signal. The sample excitation is accomplished by a supercontinuum laser source (SC-LASER) focused from the sample bottom surface. The incoming light linear polarization state is controlled by means of a linear polarizer. The signal scattered by the sample is collected with an Al-coated probe, dispersed by a spectrometer, and finally detected by a cooled InGaAs array (DTC). (b and c) RFS spectra collected when the SNOM tip is positioned on the top surface of the microring of 5 μm and 10 μm radius size, respectively, with the excitation laser polarized along the x-axis. The red and blue color highlights the two different families of peaks characterized by different Fano line shapes and different free spectral ranges. The red arrow indicates the polarization of the incident light (E_x). (d) SEM image of the investigated 5 μm radius Si microring, where the white rectangle shows the scanned area. The scale bar is 5 μm.

imaging of microresonators for both the electric[25,26] and magnetic fields.[27,28] This aspect, linked to the subwavelength spatial modulation of the mode distributions, requires using an all-optical near-field mapping technique. In waveguides (WGs) all-optical scanning near-field optical microscope (SNOM) imaging of TE and TM modes is usually performed by injecting a monochromatic laser light with the proper polarization in the WG. Different detection schemes have been proposed either by collecting the evanescent field by a near-field probe on the top surface[29−31] or by measuring the changes in the waveguide transmission resulting from the near-field perturbation by a scanning metallic probe.[32] Note that, even if the use of hyperspectral imaging is not required in WGs due to the lack of spectral resonances, it becomes very important for studying microresonators where several TE and TM modes are present. In general, TE and TM modes are usually complex to measure with a single near-field approach: some SNOM techniques are more suitable for TE modes;[33−35] others are more suitable for TM modes.[36,37] So far the near-field mapping of microring resonators has been addressed by exploiting the evanescent coupling of an external WG for loading the photons inside the microring.[13−15] Similarly to the case of isolated WGs, these results report on only one single frequency mapping. This approach requires either a particular design of the microring or a tapered fiber in close proximity to the resonator. Therefore, it cannot be easily applied to more complex circuits exhibiting several coupled photonic structures. Moreover, they did not measure the spectral properties of the modes or the spatial distribution of different polarization states in the near-field. It is worth stressing that the spectral, spatial, and polarization near-field knowledge of the TE and TM mode distributions just above the microring is of the utmost relevance for the mode coupling with emitters, since the spontaneous emission rate of a single dipole is proportional to the near-field local density of optical states projected onto the dipole direction.

Here, we report on a novel approach called the Fano-imaging technique, recently developed in ref 38. It is based on resonant light scattering combined with a polarization-controlled scanning near-field optical microscope. This scheme, by using a supercontinuum laser as excitation source, allows to perform a deep-subwavelength imaging of the modes localized in photonic crystal nanocavities, without adding any light emitter or even exploiting evanescent coupling to a waveguide.[38] In this paper, we apply the Fano-imaging technique to single and isolated microring resonators by exploiting the forward scattering configuration in order to perform a vectorial mapping in a wavelength range larger than 100 nm with a 0.11 nm spectral resolution. In addition, both excitation and detection channels are close to the microring resonator, thus avoiding the need for an additional access waveguide. Since in microrings the mode volume is quite large, the present study extends the Fano-SNOM to a wider class of systems (as compared to photonic crystal nanocavities, addressed in previous work[38]). The capability to address a single and isolated microring, which could not be characterized with another method with respect to the near-field nanoscopy, is a proof of principle that the method can address individual photonic structures and in consequence would work in all possible configurations (two or more coupled

DOI: 10.1021/acsphotonics.5b00327
ACS Photonics 2015, 2, 1712−1718

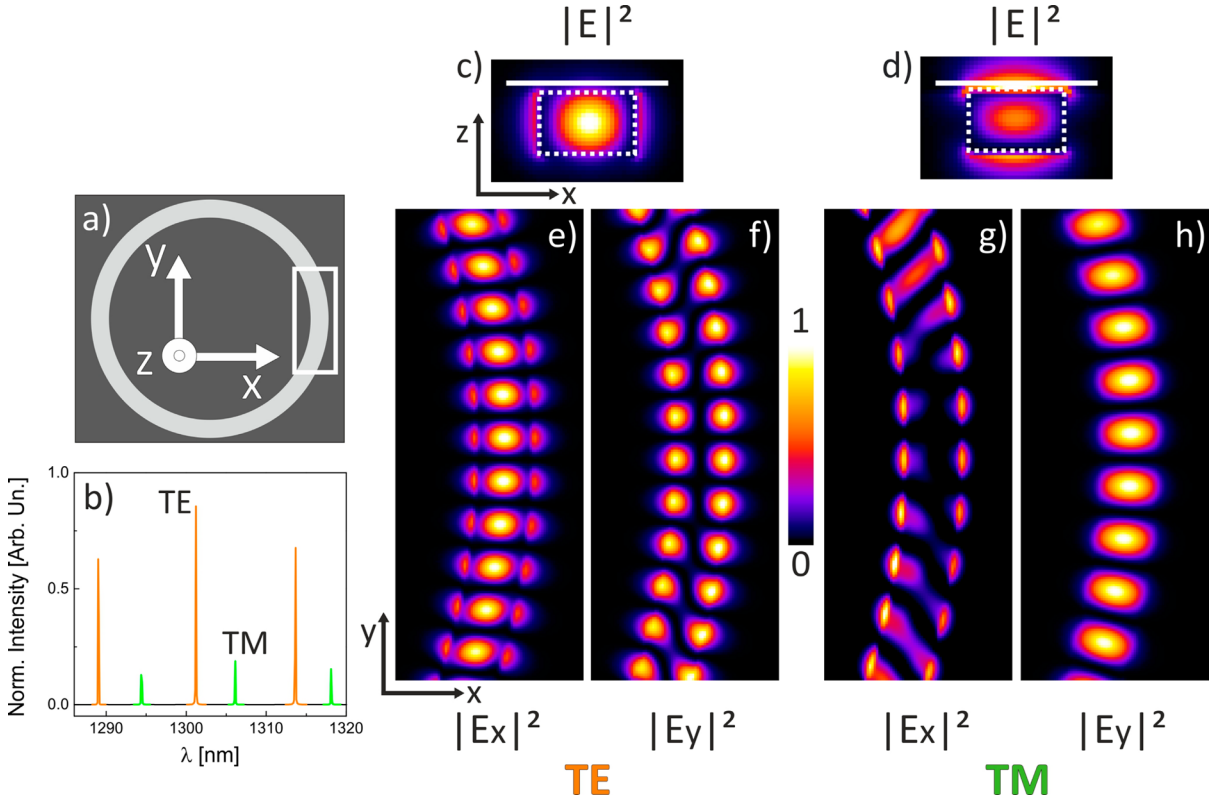

Figure 2. FDTD simulations of the TE and TM modes. (a) Schematic of the FDTD calculations. The Si ring is excited by two dipoles randomly placed polarized along *x* and *z*, respectively. In white is highlighted the longitudinal sensor area. (b) Calculated FDTD spectrum collected by the longitudinal detector. The orange and green colors highlight the TE and TM peaks characterized by different free spectral ranges. (c and d) The sensor positioned in the *xz*-plane shows the distributions of the electric field intensity $|E|^2$ calculated by FDTD of the TE and TM modes, respectively in (c) for the TE mode centered at 1301.2 nm and in (d) for the TM mode centered at 1306.1 nm. The two maps have dimensions 0.7 × 0.45 μm^2. The white dotted lines account for the core ring section (width = 350 nm and height = 220 nm), while the white line (20 nm above the ring surface) shows the profile of the sensor parallel to the ring plane. (e and f) Spatial distribution on the longitudinal sensor of the calculated *x* and *y* components of the electric field intensity for the TE mode centered at 1301.2 nm, respectively. (g and h) Spatial distribution on the longitudinal sensor of the calculated *x* and *y* components of the electric field intensity for the TM mode centered at 1306.1 nm, respectively. The maps (e)−(h) have dimensions 1.2 × 3 μm^2. All the maps are normalized to their maximum value.

microrings for instance). Our work paves the way to use near-field imaging with complex photonic circuits as a wafer testing technique. Finally, we have polarization control in the near-field, which allows us to independently measure the two in-plane polarizations of both TE and TM modes separately, addressing their character and distribution.

MATERIALS AND METHODS

Microring resonators are fabricated from SOI wafers with a 220 nm thick top Si layer and a 2 μm thick buried oxide layer, in order to give resonances in the 1300 nm wavelength range. Electron beam lithography (NanoBeam nB4, at 80 kV) is used to define the microring shape. A dry etching process with an inductively coupled plasma etcher (SF6/C4F8) transfers the patterns into the top Si layer. The microring resonators are made from a 350 nm wide waveguide bent to form a circle. We use two different ring radius sizes: 5 μm and 10 μm. The sample is covered by a thin layer of polyfluorene of refractive index around 1.6[39] deposited by spin-casting. The layer thickness was estimated by AFM and spectroscopic ellipsometry to be on the order of 5 nm.[21] A schematic view of the experimental setup in the resonant forward scattering (RFS) geometry that enables polarization control is shown in Figure 1a. The illumination is accomplished by a supercontinuum laser (SC-LASER) whose linear polarization state is controlled by a Glan-Thompson polarizing prism with an extinction ratio of approximately 3 × 10^3. The linearly polarized light is focused from the bottom surface of the sample by a 50× objective (NA = 0.45), making a spot diameter size on the order of 2 μm. The transmitted light is then collected by an Al-coated probe at about 10 nm from the top surface, dispersed by a spectrometer, and finally detected by a cooled InGaAs array (DTC). The advantage of the transmission geometry is that the excitation from the far field gives a quite strong RFS from the microring modes, which allows the use of metal-coated aperture probes, despite their low throughput. The tip and the laser excitation spot remain fixed while the sample is scanned at a constant tip−sample distance, and spectra are collected at every tip position on the sample surface. In this way, the technique ensures that the mode imaging is characterized by a deep-subwavelength spatial resolution in the full spectral range of interest within a single scan, resulting in a spatial resolution of 90 nm at 1.3 μm wavelength. In addition, the control of the polarization in the excitation path directly allows us to independently image the two TE and TM in-plane polarizations.

RESULTS AND DISCUSSION

Typical RFS spectra, spatially integrated in the azimuthal direction over a 0.05 × 0.5 μm^2 area for a better signal-to-noise ratio, are reported in Figure 1b and c for silicon microring

DOI: 10.1021/acsphotonics.5b00327
ACS Photonics 2015, 2, 1712−1718

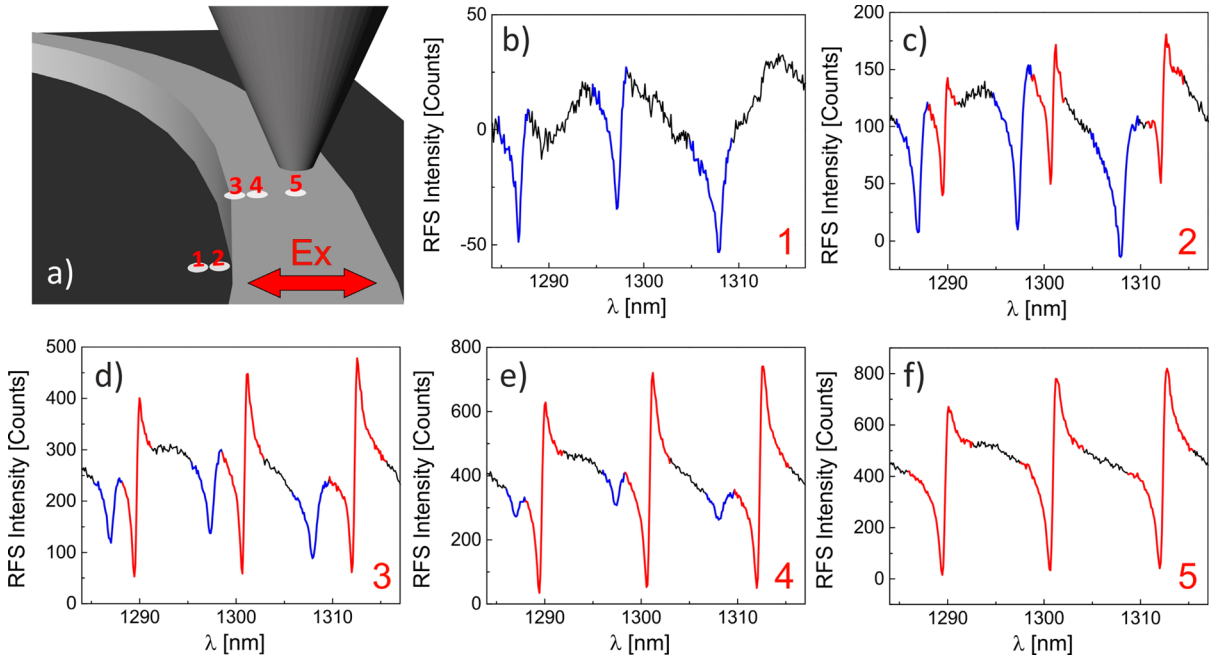

Figure 3. Spectral analysis of the TE and TM resonances. RFS spectra spatially integrated in the azimuthal direction over a 0.05 × 0.5 μm^2 area, acquired by the SNOM tip along the radial direction of the Si microring with the excitation laser polarized along the *x*-axis. (a) Schematic of the tip position on the ring. (b–f) Near-field spectra collected at different positions, as schematized in (a), with steps of 50 nm from 1 to 4 and a step of 100 nm from 4 to 5, in the radial direction. Blue resonances have maximum amplitude at the side of the structure (c, d), while the maximum of the red resonances is localized on top of the ring core (f).

resonators with a radius size of 5 μm and 10 μm, respectively, with the excitation laser polarized along the *x*-axis. Several modes are resolved in the collected spectra, and they can be fitted by Fano line shapes.[38,40] The Fano resonances in RFS measurements originate from the interference between two distinct scattering pathways: (i) light diffused forward by the surface, through a continuum of extended states, which does not interact with the cavity mode, and (ii) light resonantly coupled to the cavity mode and then scattered in free space.[38,40] This interference phenomenon gives rise to Fano resonances, whose line shapes are tightly related to the ratio between the two scattering channels. A detailed review of the theoretical analysis of the Fano line shape can be found in ref 41. The nonresonant contribution to the scattering signal, i.e., the background signal (i), is dominant in RFS measurements, and its intensity must be balanced with respect to the intensity of the resonant scattering channel (ii). This was usually performed by means of a cross-polarization detection setup, as in ref 40. However, this approach is not suitable for addressing all the relevant polarization states. On the contrary, both independent polarizations of the cavity modes can be independently measured through RFS configuration by exploiting the small-size aperture of the Al-coated probe.[38] In fact, due to the lateral Al coating, this kind of probe collects only signal coming from the small aperture at the tip apex. This effect increases the ratio between the resonant (i) and the nonresonant (ii) channels in the detection unit. In other words, the metal-coated probe offers a high spatial resolution and very efficiently filters out the nonresonant signal, thus performing near-field Fano measurements in the RFS setup for both independent polarizations.

Both RFS spectra of the microring resonators of 5 μm and 10 μm radius size display two peak sets (labeled with blue and red color), characterized by Fano-like resonances. The two sets of modes are likely related to TE and TM modes.[21] For the microring of 5 μm radius size (whose SEM image is reported in Figure 1d) the free spectral ranges (FSRs) of both peak sets are extracted from Figure 1b: they are equal to 11.5 ± 0.2 nm for the red set and 10.6 ± 0.2 nm for the blue set, in the selected spectral region. We notice that the peak sets of the 10 μm radius size ring show an FSR reduced by a factor of 2 with respect to the 5 μm radius size (see Figure 1c). In the presented experiment we observe a variation from Q = 2500 (on the mode electric field maximum) to Q = 4000 (on the mode tails), in agreement with the well-known finding that the perturbation induced by the SNOM probe affects the measured Q factor in near-field experiments.[33,27] The maximum value of Q agrees well with the Q factor of similar samples measured in the far field (i.e., without tip perturbation) by carbon nanotube photoluminescence.[21] The observed Q factor is limited by the sidewall roughness, which is not optimized for a high Q factor. Indeed, these microrings have been designed for coupling to light sources at 1300 nm,[21] and a very high Q could be detrimental for emitting devices because of the little spectral overlap with the emitters. In previous studies near-field mapping was performed at a single frequency and, consequently, the mode attribution was often tentative.[13,14] Here, we fully exploit the near-field spectral information to select the spatial mode distributions of both peak sets for a straightforward attribution. Hereafter we focus on the 5 μm radius size ring resonator to better spectrally discriminate both TE and TM modes.

For a high fidelity assessment of the TE and TM nature of the observed modes our technique is related to the comparison between the theoretical and the experimental near-field maps. The numerical calculations are performed by means of a commercially three-dimensional finite-difference time-domain (FDTD) method solver package (Crystal Wave 4.9, by Photon Design). In particular, we use the nominal parameters of the

DOI: 10.1021/acsphotonics.5b00327
ACS Photonics 2015, 2, 1712–1718

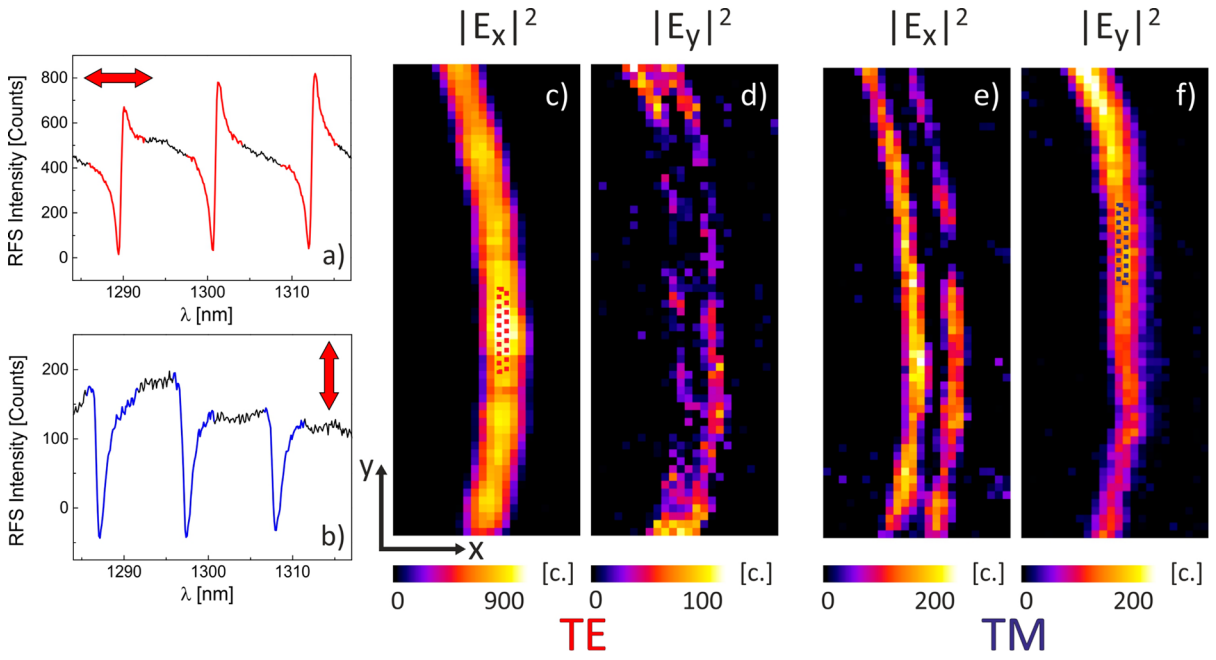

Figure 4. Resonant scattering imaging of the TE and TM modes. (a, b) Typical RFS spectra, spatially integrated on top of the ring core in the azimuthal direction over a 0.05 × 0.5 μm^2 area, with the excitation laser polarized along x and y, respectively, as indicated by the red arrows. In (c) and (f) is highlighted the integration area by the red and blue dotted lines, respectively. (c, d) SNOM maps of a red mode centered at 1301.1 nm (which eventually is a TE mode) with the excitation laser polarized along x and y, respectively. (e, f) SNOM maps of a blue mode centered at 1308.0 nm (which eventually is a TM mode) with the excitation laser polarized along x and y, respectively. All the maps have dimensions of 1.2 × 3 μm^2.

sample with a ring refractive index of 3.5, a bulk refractive index of 1.5, and a grid spacing of 15 nm. Moreover, we employ as excitation sources inside the ring resonator two randomly placed dipoles with different orientations: one parallel to the x-axis and the other parallel to the z-axis (see Figure 2a). The normalized FDTD spectrum reported in Figure 2b displays two peak sets with different FSR, labeled with orange and green color: we focus our analysis on two adjacent modes with small spectral overlap, respectively centered at 1301.2 nm and 1306.1 nm. The spatial distribution of the electric field intensity $|E|^2$ calculated by FDTD on the plane transversal to the ring for both modes is shown in Figure 2c,d. These maps show that inside the Si ring resonator the two modes have an orthogonal electric field. For the orange mode, Figure 2c, the calculated electric field intensity has a strong discontinuity on the sidewall surface, due to the fact that the electric field polarization is mainly in the ring plane (TE-like), i.e., the xy-plane, while for the green mode, Figure 2d, the calculated electric field intensity has a discontinuity on the top and bottom surface, since its polarization is mainly perpendicular to the ring plane, i.e., along the out-of-plane direction z (TM-like). Still outside the Si microring both TE and TM modes have all polarizations, and this allows us to excited them with the two in-plane polarizations x and y. We report in Figure 2e,f and g,h the x and y electric field components of the same modes calculated in the plane longitudinal to the ring plane and placed 20 nm above it. Notably, they demonstrate that a few nanometers above the ring TE and TM modes have both in-plane polarizations x and y but with different distributions. The x-polarization of the TE mode, Figure 2e, and the y-polarization of the TM mode, Figure 2h, are mainly localized along the ring core, while the y-polarization of the TE mode, Figure 2f, and the x-polarization of the TM mode, Figure 2g, are mainly localized at the edges of the ring. Note that the FDTD calculations show a stationary wave in the microring due to the presence of localized emitting dipoles, which force the two counterpropagating modes to constructively interfere at the dipole site. Finally, from these maps we find that the sharpest spatial feature of the calculated electric field distribution is as small as 60 nm. We conclude that, for a direct TE and TM mode assessment, a deep-subwavelength spatial resolution, a full spectral analysis, and a polarization control are all concurrently needed.

Therefore, we perform the Fano-imaging technique. In particular, we start by analyzing the experimental RFS spectra in the x-polarization channel as a function of the lateral distance between the tip and the ring resonator, as schematically shown in Figure 3a. The spatially resolved spectra reported in Figure 3b–f are collected in five different positions, labeled 1–5 in Figure 3a. The step between positions 1–4 is 50 nm, while the step between positions 4 and 5 is 100 nm. These spectra clearly show that the blue and red modes are localized in different regions of the microring. On the ring side the blue modes are the dominant ones and the red modes are completely missing; see Figure 3b. The opposite occurs on top of the ring core (Figure 3f), where only the red modes are present.

In order to assess the nature of the red and blue modes, we perform RFS experiments by illuminating the sample with light exhibiting the two opposite in-plane polarizations, respectively. Note that the spot diameter size on the order of 2 μm ensures an almost homogeneous excitation of the sample during SNOM scans characterized by a lateral dimension of 1.2 μm along the direction transverse to the ring. Typical RFS spectra, spatially integrated in the azimuthal direction over a 0.05 × 0.5 μm^2 area on top of the ring core for a better signal-to-noise ratio, are reported in Figure 4a,b, with the excitation laser polarized along the x- and y-axis, respectively. We report for both modes the RFS amplitude distributions, which account for the difference in counts between the maximum and the

DOI: 10.1021/acsphotonics.5b00327
ACS Photonics 2015, 2, 1712–1718

minimum of the Fano resonance. In Figure 4c,d we report on the SNOM maps of the red mode centered at 1301.1 nm, with the excitation laser polarized along the *x*- and *y*-axis, respectively. The spatial distribution of the *x*-component RFS amplitude in Figure 4c is localized in the core of the ring (where the blue modes are completely missing, as indicated by the spatially integrated spectra in Figure 4a), while the distribution of the *y*-component is localized at the edges of the structure, as reported in Figure 4d. In Figure 4e,f we report on the SNOM maps of the blue mode centered at 1308.0 nm, with the excitation light polarized along the *x*- and *y*-axis, respectively. In the latter case, the spatial distribution of the *x*-component RFS amplitude is localized at the edges of the structure, as shown in Figure 4e, while the distribution of the *y*-component is centered in the core, as shown in Figure 4f (where the red modes are completely missing, as indicated by the spatially integrated spectra in Figure 4b). The comparison with the FDTD-calculated maps of the electric field intensities for the different in-plane polarizations (see Figure 2) demonstrates that the red modes are TE-like and the blue mode are TM-like. Therefore, thanks to the good agreement with FDTD calculations, the maps collected with Al-coated tips give a high-fidelity description of the spatial distribution of the electric field intensity for any given polarization.

We notice that the experimental FSRs are larger for TE (11.5 ± 0.2 nm) than TM modes (10.6 ± 0.2 nm) in agreement with the theoretical predictions, even if the estimated FSRs from the FDTD simulation are slightly larger: 12.5 ± 0.1 nm and 11.6 ± 0.1 nm for TE and TM modes, respectively. This is probably due to a slight difference of the real dimensions (width, height, radius) of the microring from the nominal parameters.

It is worth noticing that the experimental spatial resolution as estimated by a transversal cut of the *x*-component of the TM mode gives an overall full width at half-maximum of 120 nm. This has to be compared with the 60 nm of the sharpest spatial feature of the calculated electric field distribution, and this gives a Gaussian point spread function resolution of 90 nm (approximately $\lambda/15$), after deconvolution.

CONCLUSIONS

In this paper we demonstrated that the Fano-imaging technique allows for an optical deep-subwavelength spatial resolution ($\lambda/15$), a detailed full spectral analysis, and a polarization control of Si microring photonic structures. All these properties are needed for a direct assessment of both TE and TM resonant modes, and they can also help in developing a wafer testing technique to control a specific device in a global complex circuit. The presented approach does not need the use of evanescent coupling to an adjacent waveguide either for excitation or collection. The large signal-to-noise ratio allows the use of Al-coated tips with hyperspectral mode imaging in the full spectral range of interest. Finally, we demonstrated that both TE and TM modes have in-plane electric field polarization a few nanometers outside the ring, suggesting that the ring resonators could be used for hybrid photonics together with external emitters, including quantum dots, molecules, or carbon nanotubes.[42]

AUTHOR INFORMATION

Corresponding Author

*E-mail: lachina@lens.unifi.it.

Notes

The authors declare no competing financial interest.

ACKNOWLEDGMENTS

This work was supported by the FET project FP7 618025 CARTOON. Fabrication of microring resonators was performed in the IEF cleanroom facilities (CTU/MINERVE), part of the RENATECH network. We acknowledge discussions with Francesco Riboli for mode simulation of the microring and support by Marco De Pas for fixing the electronics of the SNOM setup.

REFERENCES

(1) Purcell, E. M. Spontaneous emission probabilities at radio frequencies. *Phys. Rev.* **1946**, *69*, 681.

(2) Bayer, M.; Reinecke, T. L.; Weidner, F.; Larionov, A.; McDonald, A.; Forchel, A. Inhibition and Enhancement of the Spontaneous Emission of Quantum Dots in Structured Microresonators. *Phys. Rev. Lett.* **2001**, *86*, 3168.

(3) Yoshie, T.; Scherer, A.; Hendrickson, J.; Khitrova, G.; Gibbs, H. M.; Rupper, G.; Ell, C.; Shchekin, O. B.; Deppe, D. G. Vacuum Rabi splitting with a single quantum dot in a photonic crystal nanocavity. *Nature* **2004**, *432*, 200.

(4) Reithmaier, J. P.; Sek, G.; Löffler, A.; Hofmann, C.; Kuhn, S.; Reitzenstein, S.; Keldysh, L. V.; Kulakovskii, V. D.; Reinecke, T. L.; Forchel, A. Strong coupling in a single quantum dot−semiconductor microcavity system. *Nature* **2004**, *432*, 197.

(5) Hennessy, K.; Badolato, A.; Winger, M.; Gerace, D.; Atature, M.; Gulde, S.; Falt, S.; Hu, E. L.; Imamoglu, A. Quantum nature of a strongly coupled single quantum dot−cavity system. *Nature* **2007**, *445*, 896.

(6) Englund, D.; Faraon, A.; Fushman, I.; Stoltz, N.; Petroff, P.; Vuckovic, J. Controlling cavity reflectivity with a single quantum dot. *Nature* **2007**, *450*, 857.

(7) Posani, K. T.; Tripathi, V.; Annamalai, S.; Weisse-Bernstein, N. R.; Krishna, S.; Perahia, R.; Crisafulli, O.; Painter, O. J. Nanoscale quantum dot infrared sensors with photonic crystal cavity. *Appl. Phys. Lett.* **2006**, *88*, 151104.

(8) Anker, J. N.; Hall, W. P.; Lyandres, O.; Shah, N. C.; Zhao, J.; van Duyne, R. P. Biosensing with plasmonic nanosensors. *Nat. Mater.* **2008**, *7*, 442−453.

(9) Hausmann, B. J. M.; Bulu, I. B.; Deotare, P. B.; Mc Cutcheon, M.; Venkataraman, V.; Markham, M. L.; Twitchen, D. J.; Loncar, M. Integrated high-quality factor optical resonators in diamond. *Nano Lett.* **2013**, *13*, 1898−1902.

(10) Ritter, S.; Nolleke, C.; Hahn, C.; Reiserer, A.; Neuzner, A.; Uphoff, M.; Mucke, M.; Figueroa, E.; Bochmann, J.; Rempe, G. An elementary quantum network of single atoms in optical cavities. *Nature* **2012**, *484*, 195−200.

(11) Caselli, N.; Intonti, F.; Bianchi, C.; Riboli, F.; Vignolini, S.; Balet, L.; Li, L. H.; Francardi, M.; Gerardino, A.; Fiore, A.; Gurioli, M. Post-fabrication control of evanescent tunnelling in photonic crystal molecules. *Appl. Phys. Lett.* **2012**, *101*, 211108.

(12) Bogaerts, W.; De Heyn, P.; Van Vaerenbergh, T.; De Vos, K.; Kumar Selvaraja, S.; Claes, T.; Dumon, P.; Bienstman, P.; Van Thourhout, D.; Baets, R. Silicon microring resonators. *Laser & Photon. Rev.* **2012**, *6*, 47−73.

(13) Balistreri, M. L. M.; Klunder, D. J. W.; Blom, F. C.; Driessen, A.; Hoekstra, H. W. J. M.; Korterik, J. P.; Kuipers, L.; van Hulst, N. F. Visualizing the whispering gallery modes in a cylindrical optical microcavity. *Opt. Lett.* **1999**, *24* (24), 1829−1831.

(14) Quidant, R.; Weeber, J.-C.; Dereux, A.; Lévêque, G.; Weiner, J.; Girard, C. Addressing and imaging microring resonators with optical evanescent light. *Phys. Rev. B: Condens. Matter Mater. Phys.* **2004**, *69*, 081402 (R).

(15) Schmidt, C.; Liebsch, M.; Klein, A.; Janunts, N.; Chipouline, A.; Käsebier, T.; Etrich, C.; Lederer, F.; Kley, E.-B.; Tünnermann, A.;

DOI: 10.1021/acsphotonics.5b00327
ACS Photonics 2015, 2, 1712−1718

Pertsch, T. Near-field mapping of optical eigenstates in coupled disk microresonators. *Phys. Rev. A: At., Mol., Opt. Phys.* **2012**, *85*, 033827.
(16) Little, B. E.; Chu, S. T.; Hryniewicz, J. V.; Absil, P. P. Filter synthesis for periodically coupled microring resonators. *Opt. Lett.* **2000**, *25*, 344.
(17) Grover, R.; Absil, P. P.; Van, V.; Hryniewicz, J. V.; Little, B. E.; King, O.; Calhoun, L. C.; Johnson, F. G.; Ho, P. T. Vertically coupled GaInAsP−InP microring resonators. *Opt. Lett.* **2001**, *26*, 506.
(18) Hryniewicz, J. V.; Absil, P.P.; Little, B. E.; Wilson, R. A.; Ho, P.T. Higher order filter response in coupled microring resonators. *IEEE Photonics Technol. Lett.* **2000**, *12*, 3.
(19) Grassani, D.; Azzini, S.; Liscidini, M.; Galli, M.; Strain, M. J.; Sorel, M.; Sipe, J. E.; Bajoni, D. Micrometer-scale integrated silicon source of time-energy entangled photons. *Optica* **2015**, *2*, 88−94.
(20) Gaufrès, E.; Izard, N.; Noury, A.; Le Roux, X.; Rasigade, G.; Beck, A.; Vivien, L. Light Emission in Silicon from Carbon Nanotubes. *ACS Nano* **2012**, *6*, 3813.
(21) Noury, A.; Le Roux, X.; Vivien, L.; Izard, N. Controlling carbon nanotube photoluminescence using silicon microring resonators. *Nanotechnology* **2014**, *25*, 215201.
(22) Kasperczyk, M.; Person, S.; Ananias, D.; Carlos, L. D.; Novotny, L. Excitation of Magnetic Dipole Transitions at Optical Frequencies. *Phys. Rev. Lett.* **2015**, *114*, 163903.
(23) Morichetti, F.; Canciamilla, A.; Ferrari, C.; Torregiani, M.; Melloni, A.; Martinelli, M. Roughness induced backscattering in optical silicon waveguides. *Phys. Rev. Lett.* **2010**, *104*, 033902.
(24) Barwicz, T.; Watts, M. R.; Popović, M. A.; Rakich, P. T.; Socci, L.; Kärtner, F. X.; Ippen, E. P.; Smith, H. I. Polarization-transparent microphotonic devices in the strong confinement limit. *Nat. Photonics* **2007**, *1*, 57−60.
(25) Mintairov, A. M.; Chu, Y.; He, Y.; Blokhin, S.; Nadtochy, A.; Maximov, M.; Tokranov, V.; Oktyabrsky, S.; Metz, J. L. High-spatial-resolution near-field photoluminescence and imaging of whispering-gallery modes in semiconductor microdisks with embedded quantum dots. *Phys. Rev. B: Condens. Matter Mater. Phys.* **2008**, *77*, 195322.
(26) Vignolini, S.; Intonti, F.; Riboli, F.; Wiersma, D. S.; Balet, L.; Li, L. H.; Francardi, M.; Gerardino, A.; Fiore, A.; Gurioli, M. Polarization-sensitive near-field investigation of photonic crystal microcavities. *Appl. Phys. Lett.* **2009**, *94*, 163102.
(27) Vignolini, S.; Intonti, F.; Riboli, F.; Balet, L.; Li, L. H.; Francardi, M.; Gerardino, A.; Fiore, A.; Wiersma, D. S.; Gurioli, M. Magnetic imaging in photonic crystal microcavities. *Phys. Rev. Lett.* **2010**, *105*, 123902.
(28) Caselli, N.; La China, F.; Bao, W.; Riboli, F.; Gerardino, A.; Li, L.; Lienfield, E. H.; Pagliano, F.; Fiore, A.; Schuck, P. J.; Cabrini, S.; Weber-Bargioni, A.; Gurioli, M.; Intonti, F. Deep-subwavelength imaging of both electric and magnetic localized optical fields by plasmonic campanile nanoantenna. *Sci. Rep.* **2015**, *5*, 9606.
(29) Tortora, P.; Abashin, M.; Märki, I.; Nakagawa, W.; Vaccaro, L.; Salt, M.; Herzig, H. P.; Levy, U.; Fainman, Y. Observation of amplitude and phase in ridge and photonic crystal waveguides operating at 1.55 μm by use of heterodyne scanning near-field optical microscopy. *Opt. Lett.* **2005**, *30*, 2885.
(30) Stern, L.; Desiatov, B.; Goykhman, I.; Lerman, G. M.; Levy, U. Near field phase mapping exploiting intrinsic oscillations of aperture NSOM probe. *Opt. Express* **2011**, *19*, 12014−12020.
(31) Bozhevolnyi, S. I.; Volkov, V. S.; Søndergaard, T.; Boltasseva, A.; Borel, P. I.; Kristensen, M. Near-field imaging of light propagation in photonic crystal waveguides: Explicit role of Bloch harmonics. *Phys. Rev. B: Condens. Matter Mater. Phys.* **2002**, *66*, 235204.
(32) Robinson, J. T.; Preble, S. F.; Lipson, M. Imaging highly confined modes in sub-micron scale silicon waveguides using Transmission-based Near-field Scanning Optical Microscopy. *Opt. Express* **2006**, *14* (22), 10588−10595.
(33) Intonti, F.; Vignolini, S.; Riboli, F.; Vinattieri, A.; Wiersma, D. S.; Colocci, M.; Balet, L.; Monat, C.; Zinoni, C.; Li, L. H.; Houdré, R.; Francardi, M.; Gerardino, A.; Fiore, A.; Gurioli, M. Spectral tuning and near-field imaging of photonic crystal microcavities. *Phys. Rev. B: Condens. Matter Mater. Phys.* **2008**, *78*, 041401(R).
(34) le Feber, B.; Rotenberg, N.; Beggs, M.; Kuipers, L. Simultaneous measurement of nanoscale electric and magnetic optical fields. *Nat. Photonics* **2014**, *8*, 43−46.
(35) Dellinger, J.; Van Do, K.; Le Roux, X.; de Fornel, F.; Cassan, E.; Cluzel, B. Hyperspectral optical near-field imaging: Looking graded photonic crystals and photonic metamaterials in color. *Appl. Phys. Lett.* **2012**, *101*, 141108.
(36) Sapienza, R.; Coenen, T.; Renger, J.; Kuttge, M.; van Hulst, N. F.; Polman, A. Deep-subwavelength imaging of the modal dispersion of light. *Nat. Mater.* **2012**, *11*, 781−787.
(37) Schnell, M.; García-Etxarri, A.; Huber, A. J.; Crozier, K.; Aizpurua, J.; Hillenbrand, R. Controlling the near-field oscillations of loaded plasmonic nanoantennas. *Nat. Photonics* **2009**, *3*, 287−291.
(38) Caselli, N.; Intonti, F.; La China, F.; Riboli, F.; Gerardino, A.; Bao, W.; Weber-Bargioni, A.; Li, L.; Linfield, E. H.; Pagliano, F.; Fiore, A.; Gurioli, M. Ultra-subwavelength phase sensitive Fano-imaging of localized photonic modes. *Light: Sci. Appl.* **2015**, *4*, e326.
(39) Campoy-Quiles, M.; Etchegoinb, P. G.; Bradleya, D. D. C. Exploring the potential of ellipsometry for the characterisation of electronic, optical, morphologic and thermodynamic properties of polyfluorene thin films. *Synth. Met.* **2005**, *155*, 279.
(40) Galli, M.; Portalupi, S. L.; Belotti, M.; Andreani, L. C.; O'Faolain, L.; Krauss, T. F. Light scattering and Fano resonances in high-Q photonic crystal nanocavities. *Appl. Phys. Lett.* **2009**, *94* (7), 071101.
(41) Miroshnichenko, A. E.; Flach, S.; Kivshar, Y. S. Fano resonances in nanoscale structures. *Rev. Mod. Phys.* **2010**, *82*, 2257.
(42) Prabhakaran, P.; Kim, W. J.; Lee, K. S.; Prasad, P. N. Quantum dots (QDs) for photonic applications. *Opt. Mater. Express* **2012**, *2*, 578.

DOI: 10.1021/acsphotonics.5b00327
ACS Photonics 2015, 2, 1712−1718